INSIGHTS INTO THE PHYSICAL CONDITIONS AND INTERNAL STRUCTURE OF A CANDIDATE PROTO-GLOBULAR CLUSTER

Molly K. Finn
Astronomy Department, University of Virginia, Charlottesville, VA 22904

We present $\sim$ 0.1" resolution ($\sim$ 10 pc) ALMA observations of a molecular cloud identified in the merging Antennae galaxies with the potential to form a globular cluster, nicknamed the "Firecracker." Since star formation has not yet begun at an appreciable level in this region, this cloud provides an example of what the birth environment of a globular cluster may have looked like before stars form and disrupt the natal physical conditions. Using emission from ^{12}CO(2-1), ^{12}CO(3-2), and ^{13}CO(2-1) molecular lines, we are able to resolve the cloud's structure and find that it has a characteristic radius of 22 pc and a mass of 1–9$\times10^6 M_\odot$. We demonstrate that if the cloud is bound (as is circumstantially suggested by its bright, compact morphology), an external pressure in excess of $P/k > 10^8$ K cm^{-3} is required. This would be consistent with theoretical expectations that globular cluster formation requires high pressure environments, much higher than typical values found in the Milky Way. The position-velocity diagram of the cloud and its surrounding material suggests that this high pressure may be produced by ram pressure from the collision of filaments.

1. Introduction

As some of the oldest objects in the universe, globular clusters are important probes of the early stages of galaxy formation and evolution. They are abundant in all massive galaxies, despite theoretical predictions that they have a high mortality rate, with potentially $\lesssim 1\%$ surviving to 10 Gyr (Fall & Zhang, 2001). This suggests that the star formation process that created globular clusters was abundant in the early universe.

The discovery of young, dense star clusters in nearby galaxies, dubbed "super star clusters" (SSCs), provided evidence that this star formation process is still occurring in the present universe (O'Connell et al., 1994). Further studies imply that these SSCs are likely very similar to the progenitors of the ancient globular clusters we are familiar with (McLaughlin & Fall, 2008), though most will not survive to >10 Gyr. These clusters are primarily observed at optical and UV wavelengths, so most of our knowledge is confined to stages of evolution that occur after the progenitor cloud has formed stars and the cluster has at least partially emerged from its nascent molecular cloud.

To observe the earliest stages of formation and evolution, we need to look at millimeter wavelengths that can see the structure of the molecular clouds, before stars have formed and while the birth environment is still intact. This stage of formation is expected to be short-lived, lasting only $\sim 0.5 - 1$ Myr (Johnson et al., 2015), and so these objects are expected to be rare and therefore difficult to find.

To form a globular cluster, a molecular cloud must have a sufficiently large mass within a relatively small radius. If we take the typical globular cluster to have a half-light radius of $\lesssim$10 pc (van den Bergh et al., 1991) and a stellar mass of $\gtrsim 10^5 M_\odot$ (Harris & Pudritz, 1994), and assuming a star formation efficiency (SFE) of $20 - 50\%$ (Ashman & Zepf, 2001; Kroupa et al., 2001), then if a globular cluster loses approximately half its mass over the course of 10 Gyr, the progenitor molecular cloud must have an initial mass of $\gtrsim 10^6 M_\odot$ and a radius of < 25 pc (Johnson et al., 2015). To constrain the evolutionary stage of the cluster to before the onset of star formation, the cloud must also have no associated thermal radio emission, which would penetrate the surrounding mate-

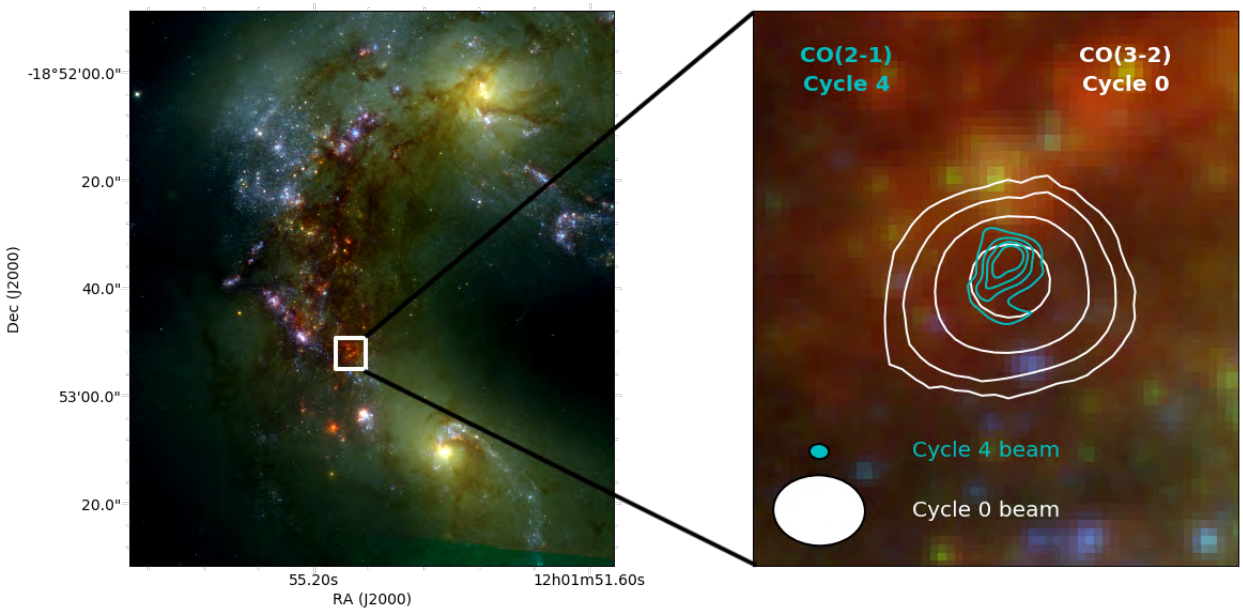

Figure 1: *Left*: Three-color Hubble Space Telescope image of the Antennae galaxies. *Right*: Proto-SSC in the Overlap region with CO(3-2) moment 0 contours (0.4, 0.8, 1.6, 3.2 Jy beam^{-1} km s^{-1}, white) from Johnson et al. (2015) ALMA Cycle 0 data, and CO(2-1) moment 0 contours (10, 15, 20, 25σ, $\sigma = 0.04$ Jy beam^{-1} km s^{-1}, cyan) from ALMA Cycle 4. The synthesized beams for the Cycle 0 and Cycle 4 data are 0.43"×0.56" (46×60 pc) and 0.09"×0.12" (10×13 pc) respectively.

rial and indicate that stars have formed and begun ionizing the surrounding gas.

We also expect that a molecular cloud forming a massive star cluster must be subject to a high external pressure. Elmegreen & Efrefmov (1997) show that globular clusters with masses of $> 10^5 M_\odot$ and core radii of 1-10 pc would require an external pressure of $P_0/k \sim 10^7 - 10^9$ K cm^{-3} during formation for the resulting object to be bound. This pressure is orders of magnitude larger than typical ISM pressures in the disc of the Milky Way, and is likely to only be achieved in particular scenarios, including interactions between galaxy systems. This makes the merging Antennae galaxies, where high densities and pressures as well as an abundant population of optically-visible SSCs have been observed (Whitmore, 2000), a prime location to search for such a molecular cloud. At a distance of 22 Mpc, it is also close enough that with ALMA, we are now able to resolve size scales that are comparable to those of the precursor molecular clouds which could generate globular clusters.

Using data from an ALMA Early Science project, Whitmore et al. (2014) found a candidate pre-SSC cloud in the overlap region of the Antennae using CO(3-2) with a beam size of 0.56"×0.43". Follow up analysis by Johnson et al. (2015) characterized it as having an inferred mass of 3.3–15×10$^6 M_\odot$, a deconvolved radius of $< 24 \pm 3$ pc, and a pressure of $P_0/k \gtrsim 10^9$ K cm^{-1}, all of which are consistent with expectations for a SSC-forming cloud. It also has no detectable associated thermal radio emission, where the upper limit on the peak ionizing flux from Johnson et al. (2015) is $N_{\rm Lyc} \approx 6 \times 10^{50}$ s^{-1}, which corresponds to ~ 60 O-type stars, or M$_* \lesssim 10^4 M_\odot$, which is more than two orders of magnitude less than the inferred mass of the cloud. Given that the expected resultant cluster will have a mass of $M_* > 10^5 M_\odot$, this is taken to indicate that the Firecracker is likely to still be in a very early

stage of formation. Johnson et al. (2015) also demonstrate that the cloud is most likely supported by turbulence, and so on a timescale of $\sim$ 1 Myr this turbulence will dissipate, initiating collapse if the cloud is bound, or dispersal if it is not.

This cloud has been nicknamed the "Firecracker," and to the best of our knowledge, is the only example found thus far that has the potential to be in the earliest stages of forming a massive star cluster with the potential to evolve into a globular cluster. Some very young SSCs have been identified with associated molecular gas (e.g. Leroy et al., 2018; Turner et al., 2017; Oey et al., 2017), but all of these also have associated thermal radio emission indicative of stars having formed. With the exception of one source from Leroy et al. (2018), this star formation is above the detection threshold for the Firecracker cloud.

Here we present new, high resolution ALMA observations of ^{12}CO(2-1), ^{12}CO(3-2), and ^{13}CO(2-1) emission that are capable of resolving the structure of the Firecracker cloud and improve upon the previous characterization of the source (Figure 1). The combination of the optically thick ^{12}CO and the optically thin ^{13}CO allow us to more directly measure the mass, while the improved resolution permits a more accurate size measurement for the cloud.

2. Observations

We observed the overlap region of the Antennae galaxies using ALMA Band 6 and Band 7 in both extended and compact configurations during ALMA Cycles 3 and 4 (program codes 2015.1.00977.S and 2016.1.00924.S). These observations included continuum emission at each frequency, as well as emission from ^{12}CO(2-1), ^{12}CO(3-2), and ^{13}CO(2-1).

In the vicinity of the Firecracker, there is diffuse continuum emission at all three frequencies throughout the area, associated with the SGMCs in the overlap region. However, there is no peak in emission or any morphology in the continuum associated with the Firecracker itself, based on the well-detected CO emission (see Figure **??**). We therefore consider this a non-detection of the Firecracker, with 5σ upper limits for the peak emission of 3.0×10^{-4} Jy beam^{-1} at 349 GHz, 9.5×10^{-5} Jy beam^{-1} at 237 GHz, and 6.0×10^{-5} Jy beam^{-1} at 226 GHz. The Firecracker cloud was detected strongly in ^{12}CO(2-1), ^{12}CO(3-2), and ^{13}CO(2-1), and the parameters of the data cubes for each detected transition are summarized in Table **??**.

Transition	Synth. Beam (arcsec^2)	RMS/chan (mJy/beam)
^{12}CO(2-1)	0.09×0.12	0.6
^{12}CO(3-2)	0.15×0.16	2.0
^{13}CO(2-1)	0.17×0.18	0.25

Table 1: Data cube parameters for detected transitions in the Firecracker region

3. Analysis

3.1 Moment Maps

After extracting the Firecracker from the surrounding field, we made total intensity maps (moment 0), integrating over the velocity range 1430-1555 km s^{-1}, and peak intensity maps (moment 8) for ^{12}CO(2-1), ^{12}CO(3-2), and ^{13}CO(2-1). The total intensity (moment 0) and peak intensity (moment 8) maps for each CO transition are shown in Figure 2.

To determine the size of the cloud from these observations, we use the ^{13}CO(2-1) emission, since it is optically thin and gives a better representation of the cloud's structure than the optically thick ^{12}CO. We define a characteristic radius, which is the radius of a circle with the same area as that enclosed by the 5σ contour of the ^{13}CO(2-1) total intensity (moment 0) map. This characteristic radius for the Firecracker is

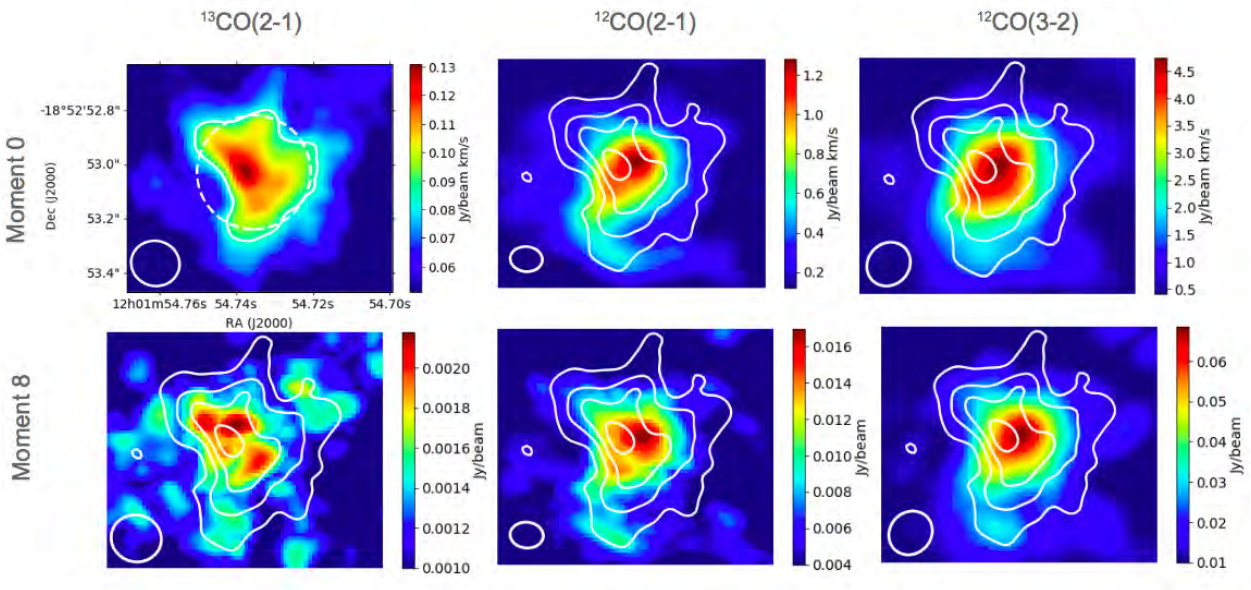

Figure 2: *Top row*: Total intensity (moment 0) maps. *Bottom row*: Peak intensity (moment 8) maps. *Left column*: ^{13}CO(2-1). *Middle column*: ^{12}CO(2-1). *Right column*: ^{12}CO(3-2). In the ^{13}CO(2-1) moment 0 image (upper left), the solid white line represents the 5σ (σ=0.017 Jy beam^{-1} km s^{-1}) contour, and the dashed white line represents the circle with area equal to that enclosed by the 5σ contour. The radius of this circle is 0.21", which is taken to be the characteristic radius of the cloud. In the other images, contours of the ^{13}CO(2-1) are overplotted at 4, 5, 6, and 7σ levels. Synthesized beams are shown in the bottom left corners of each image, and are 0.17"×0.18" for ^{13}CO(2-1), 0.09"×0.12" for ^{12}CO(2-1), and 0.15"×0.16" for ^{12}CO(3-2).

0.21", which corresponds to a size of 21 pc at a distance of 22 Mpc.

3.2 Cloud Mass

Observations of both ^{12}CO(2-1) and ^{13}CO(2-1) allow us to determine the optical depth of the cloud by assuming an abundance ratio for these two molecules and assuming that their excitation temperatures are the same.

In the overlap region of the Antennae, the ^{12}CO/^{13}CO abundance ratio has been measured to be $X_{12}/X_{13} \simeq 70$, though it is poorly constrained in this region and could vary from 40 to 200 (Zhu et al., 2003). We convolved the ^{12}CO(2-1) image to the synthesized beam of ^{13}CO(2-1), then fit Gaussian profiles to the velocity profile for each ^{12}CO(2-1) pixel. We then fit Gaussian profiles to the ^{13}CO(2-1) velocities, fixing the central velocity to be the same as the corresponding ^{12}CO(2-1) pixel, and masking pixels where a solution to the fit could not be found. Taking the ratio of the peak brightness temperatures of these two molecular lines at each unmasked pixel, we created a map of the peak optical depth, τ_{12}, using the equation

$$\frac{T_{12}}{T_{13}} = \frac{T_{x,12}}{T_{x,13}} \frac{1-e^{-\tau_{12}}}{1-e^{-\tau_{13}}} = \frac{1-e^{-\tau_{12}}}{1-e^{-\tau_{13}}}, \qquad (1)$$

by taking $\tau_{12}/\tau_{13} = X_{12}/X_{13}$ and assuming that the excitation temperatures for ^{12}CO and ^{13}CO are equal ($T_{x,12} = T_{x,13}$). From these optical depths, we found the peak excitation temperature, T_x, at each pixel given by

$$T_{12} = (1-e^{-\tau_{12}}) \frac{T_{\rm UL}}{e^{T_{\rm UL}/T_x} - 1}, \qquad (2)$$

where $T_{\rm UL} = 11.07$ K for ^{12}CO.

We then determined τ_{12} for each velocity in the cube, giving us a profile of the optical depth for each pixel. This was done by using Equation 1 with the ratio of the brightness temperature of ^{12}CO(2-1) and ^{13}CO(2-1) wherever ^{13}CO(2-1) was detected ($> 4\sigma$, σ = 0.02 K). Where ^{13}CO(2-1) was not detected and ^{12}CO(2-1) was detected, we used Equation 2 with the brightness temperature of ^{12}CO(2-1) only, and assuming that the excitation temperature does not vary with velocity. The data cubes were masked with thresholds of 3σ (σ = 0.6 mJy beam^{-1} for ^{12}CO(2-1) and σ = 0.25 mJy beam^{-1} for ^{13}CO(2-1)). With the assumption that the excitation temperature remains constant at all velocities within the cloud, we found the column density at each pixel using the equation from Mangum & Shirley (2015):

$$N_{tot} = \frac{8\pi\nu_0^2 Q}{c^2 A_{ul} g_u} e^{\frac{E_u}{kT_x}} \left(e^{\frac{h\nu_0}{kT_x}} - 1\right)^{-1} \int_0^\infty \tau_\nu d\nu \tag{3}$$

For ^{12}CO, this equation becomes

$$\frac{N_{tot}^{12}}{\text{cm}^{-2}} = 3.3{\times}10^{14} \left(\frac{T_x}{B_0} + \frac{1}{3}\right) \frac{1}{e^{\frac{-5.53}{T_x}} - e^{\frac{-16.6}{T_x}}} \int_0^\infty \tau_v dv \tag{4}$$

where $B_0 = 2.7674$ K for ^{12}CO.

From these column densities, we take an $H_2/^{12}$CO abundance ratio of $H_2/^{12}$CO = $10^4 - 10^5$, which is typical of Milky Way IRDCs, before or slightly after protostellar objects have formed, akin to the stage we expect the Firecracker to most likely be in (Gerner et al., 2014). We then assume the total mass is 1.3 times the mass of H_2 to derive the total mass surface density (shown as a map in Figure 3). Taking a pixel area of A = 2.23 pc^2, we can add the mass from each pixel to get the total mass of the cloud.

Different combinations of values in the expected ranges of X_{12}/X_{13} and $H_2/^{12}$CO were used, resulting in masses that varied in the range 1.0–31$\times10^6 M_\odot$. In Section **??**, we will put additional constraints on the upper limit of this mass range due to dust emission. Mass estimates for a few selected parameter combinations are given in Table **??**. The mass directly tracks variations in $H_2/^{12}$CO, with an order of magnitude change in $H_2/^{12}$CO corresponding to an order of magnitude change in mass. The resulting mass is less sensitive to X_{12}/X_{13}, with a factor of five change in this value only resulting in a factor of ~ 3 change in mass.

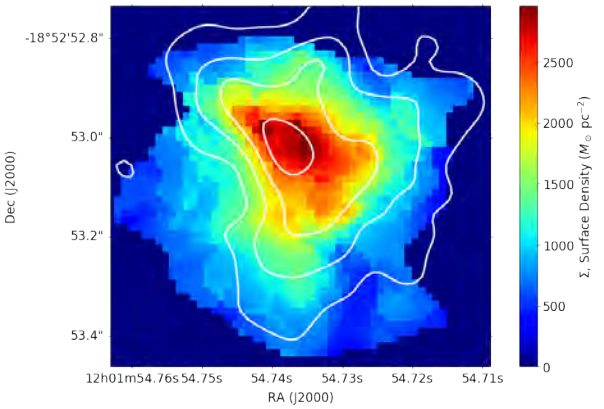

Figure 3: Map of the mass surface density. This version was created with the assumed parameters X_{12}/X_{13} = 70 and $H_2/^{12}$CO= $10^{4.5}$. Summing over all the pixels and assuming a pixel area of 2.23 pc^2 results in a total mass of $4.5 \times 10^6 M_\odot$. Overplotted are contours of ^{13}CO(2-1) moment 0.

		X_{12}/X_{13} =			
		40	70	120	200
$H_2/^{12}$CO =	10^4	1.0	1.4	2.1	3.1
	$10^{4.5}$	3.3	4.5	6.5	9.7
	10^5	11	14	21	31

Notes. Masses for given combinations of X_{12}/X_{13} and $H_2/^{12}$CO assumptions are given in the body of the table with units of $10^6 M_\odot$.

Table 2: Possible values for the mass ($10^6 M_\odot$)

3.3 Expected Continuum Emission

The lack of detected continuum emission associated with the Firecracker sets further constraints on the mass of the cloud. At all three

frequencies, there is diffuse continuum emission associated with the larger region, but no morphology or peak emission associated with Firecracker above 3.8σ (Figure **??**). We consider this a non-detection of the Firecracker, and use the integrated flux from the diffuse emission to set an upper limit on the Firecracker's dust mass.

Using the Band 7 observations (in which the dust emission from the Firecracker should be brightest), we flagged the emission lines to create a continuum image with a beam FWHM of 0.17"×0.21" and an RMS of 0.06 mJy beam^{-1}. The integrated flux in a 0.35" radius circular region around the Firecracker is $S_{880} = 0.78 \pm 0.2$ mJy.

From Wilson et al. (2008),

$$M_{dust} = 74,220 S_{880} D^2 \frac{(e^{17/T} - 1)}{\kappa} (M_\odot), \quad (5)$$

where S_{880} is measured in Janskys at 880μm (Band 7), D is measured in Mpc, κ is the dust emissivity measured in cm^2 g^{-1}, and T is measured in K. For the Antennae system, $D = 22$ Mpc. Taking $T_{Kin} \simeq T_{ex}$, the temperature measured in this region is 25–35 K. Typical values adopted for the dust emissivity and gas-to-dust ratio in these types of environments are $\kappa = 0.9 \pm 0.13$ cm^2 g^{-1} and a ratio of 120 ± 28 (Wilson et al., 2008).

If we take the most extreme values to maximize M_{dust} within the expected range for each parameter (so $S_{880} \leq 1.34$ mJy, $T \geq 25$ K, $\kappa \geq 0.77$ cm^2 g^{-1}), the upper limit on the dust mass would be $M_{dust} \leq 6 \times 10^4 M_\odot$. Taking the maximum gas-to-dust ratio ≤ 148, the largest total mass that would be consistent with the continuum non-detection would be $9 \times 10^6 M_\odot$. This is then taken as the upper limit on the mass of the Firecracker.

3.4 Cloud Pressure

We examine the effect of the cloud's environment on the parameters derived thus far by comparing the surface density, Σ, to a size-linewidth coefficient, σ_V^2/R. The velocity dispersions were determined by fitting a Gaussian profile to the ^{12}CO(3-2) emission line. The radius is taken to be the size of the aperture being measured, and the surface density is taken as the average within that aperture, based on the range of mass maps derived in Section **??**.

We determine these parameters for four different apertures, shown in the right panel of Figure 4. The largest, Aperture 4, is selected to include all ^{13}CO(2-1) emission above $\approx 4\sigma$, with a radius of 0.35" (37 pc). The next, Aperture 3, is selected to approximately match the size of the 5σ contour of the ^{13}CO(2-1), with a radius of 0.24" (26 pc). The next, Aperture 2, is selected to approximately follow the contour of 6σ emission, with a radius of 0.14" (15 pc). Aperture 1 is approximately the ^{12}CO(2-1) beam size, with a radius of 0.06" (6.4 pc).

From the left panel of Figure 4, these parameters indicate that the cloud is neither in virial equilibrium nor in free fall, implying that to be bound (as circumstantially suggested by its morphology), the cloud must be subject to a high external pressure with $P_e/k \gtrsim 10^8$ K cm^{-3}. This would agree with previous analysis by Johnson et al. (2015), the fit of the Bonnor-Ebert profile in Section **??**, and theoretical expectations for cluster formation (Elmegreen & Efrefmov, 1997).

Furthermore, we see that the inferred pressure increases as the aperture radius decreases, zooming in on the central region of the cloud. This may be an indication that we are tracing an internal pressure structure. It also may, however, be a measurement effect, since the radius of the selected aperture may not be a good indicator of the bound radius in the given region.

Also compared in the leftmost panel of Figure 4 young massive clusters discovered by Leroy et al. (2018) in NGC 253, for which star formation has been detected. These clusters include both a gas and stellar mass component (with gas masses in the range $10^{3.6}$ –

$10^{5.7} M_\odot$, and stellar masses in the range $10^{4.1} - 10^{6.0} M_\odot$), and we also compare the ratio $M_{\rm gas}/M_*$ to their position in this plot. Most of the clusters fall along either the free fall or virial equilibrium lines, but one notable cluster with a significantly higher $M_{\rm gas}/M_*$ than all of the other clusters is above these lines, suggesting a high external pressure ($P_e/k \gtrsim 10^9$ K cm^{-3}) would be required to keep it bound. Another cluster with a more modestly enhanced $M_{\rm gas}/M_*$ is also above virial and free fall lines. This may be an indication that the pressure environment of massive clusters is correlated with the evolutionary stage of the cluster. This would support a scenario in which clusters form in high pressure environments, then the pressure dissipates or is dispelled as stars form and the cluster emerges.

3.5 Kinematics of the Local Environment

To examine the larger local environment that may be causing the high external pressure derived above, we look at the kinematics of the surrounding region. If the source of pressure is ram pressure from the collision of molecular clouds, we might expect to see a "broad bridge" feature connecting the two clouds in the position-velocity diagram, as described by Haworth et al. (2015).

Using ^{12}CO(2-1) emission of the Firecracker and the surrounding giant molecular cloud, we created a total intensity (moment 0) map by integrating over the velocity range 1430–1555 km s^{-1}, and a mean velocity (moment 1) map using a 0.6 mJy threshold. These maps were used to choose an angle and cut for a position-velocity diagram that would capture the proposed collision axis where the velocity gradient is greatest. These cuts and the resulting position-velocity diagram are shown in Figure 5.

The Firecracker does appear as a bridge between the two adjacent clouds, although it appears somewhat spatially separated from each. Its morphology is different from that of the broad bridge feature from Haworth et al. (2015), but this may be due to a difference in viewing angle, as the line-of-sight of the simulated position-velocity diagrams from Haworth et al. (2015) were made directly along the collision axis. This would seem to suggest that cloud-cloud collision is likely occurring, and may be the source of pressure that we observe.

4. Discussion

To determine the source of the high external pressure implied by Figure 4 and the Bonnor-Ebert fit, we look to the encompassing cloud and its kinematics. Johnson et al. (2015) estimate that the weight of the surrounding super giant molecular cloud would only reach $P/k \sim 10^7$ K cm^{-3}. This falls short of the expected external pressure by one or two orders magnitude.

One mechanism that may be able to increase the pressure in the region to the values we observe is ram pressure from colliding filaments. The Firecracker cloud is located at the confluence of two CO filaments identified by Whitmore et al. (2014), the region has a large velocity gradient across it, and is associated with strong H_2 emission (Herrera et al., 2011, 2012). Work by Wei et al. (2012) also shows that the overlap region may be dominated by compressive shocks. All of these would be consistent with collisions causing the high external pressure observed for the Firecracker cloud. Furthermore, the now-resolved irregular structure of the cloud is consistent with the source of pressure being non-isotropic, as we would expect in the case of colliding gas filaments.

Examination of the position-velocity diagram (Figure 5) shows a hint of a "broad bridge" feature, described by Haworth et al. (2015) to be a signature of cloud-cloud collision. If this is indeed a case of cloud-cloud collision, we can determine the density of the clouds on either side of the Firecracker. Assuming that the cross sections along the line of

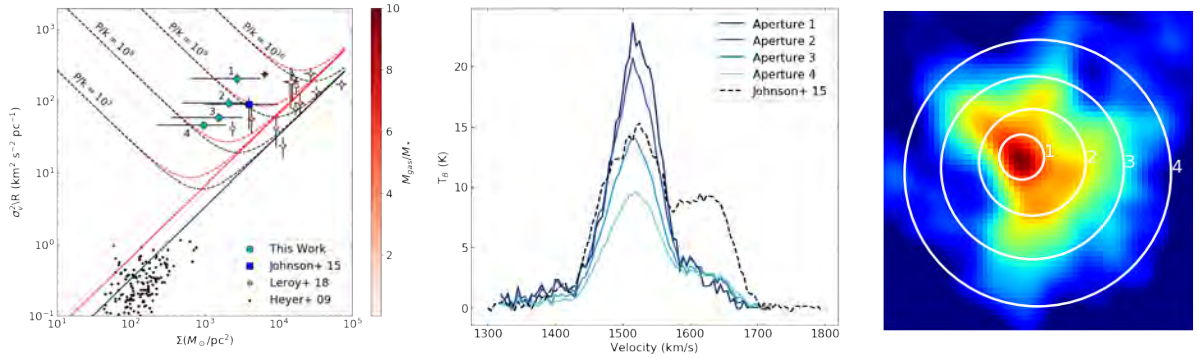

Figure 4: *Left*: The size-linewidth coefficient (σ_V^2/R) and surface density (Σ) for the Firecracker cloud as measured in different apertures (cyan circles) and in previous analysis by Johnson et al. (2015) (blue square). Also shown are young massive clusters from Leroy et al. (2018) in NGC 253, colored based on the ratio of $M_{\rm gas}/M_*$, and typical molecular clouds observed in the Milky Way by Heyer et al. (2009) for comparison (black circles). The black line corresponds to virial equilibrium, while the red lines correspond to free fall conditions (Field et al., 2011). The position of the Firecracker cloud suggests that it must be subject to a high external pressure ($\gtrsim 10^8$ K cm^{-3}, dotted lines) to remain bound. *Center*: The ^{12}CO(3-2) line profiles in each of the four regions as well as from previous analysis by Johnson et al. (2015) (dashed line). *Right*: The four chosen apertures plotted on the ^{13}CO(2-1) moment 0 map. These have radii of 0.06", 0.14", 0.24", and 0.35" for Apertures 1, 2, 3, and 4, which correspond to sizes of 6.4, 15, 26 and 37 pc respectively.

sight of the colliding clouds are twice the Firecracker's diameter, so have a depth of 88 pc, we find that the density of the colliding clouds is approximately $\rho \sim 10^{-21}$ g cm^{-3} ($n_{H_2} \sim 220$ cm^{-3}).

From Figure 5, the velocities of the two colliding clouds are approximately 1465 km s^{-1} and 1590 km s^{-1}, suggesting that the projected velocity difference at which they would be colliding is $v \sim 125$ km s^{-1}. Taking the ram pressure to be $P = \rho v^2$, this would imply that the pressure caused by such a cloud-cloud collision would be $P/k \sim 1.1 \times 10^9$ K cm^{-3}. While this is a fairly rough estimate of the ram pressure, it demonstrates that such a scenario would be capable of providing the high external pressures required for the Firecracker cloud to be bound.

5. Conclusions

We present ALMA observations of the proto-SSC Firecracker cloud in the overlap region of the Antennae, looking at emission from ^{12}CO(2-1), ^{12}CO(3-2), ^{13}CO(2-1), HCN(4-3), and HCO$^+$(4-3). These molecular lines were used to characterize the cloud and the surrounding environment at resolutions as low as ~ 0.1" (10 pc). The findings are summarized below.

- We determine the mass of the cloud to be in the range 1–9$\times 10^6 M_\odot$ and its characteristic radius is 22 pc. These both agree with previous measurements by Johnson et al. (2015) and are consistent with the cloud having the potential to form a super star cluster.

- We do not detect continuum emission at any of the three observed frequencies. This allows us to put an upper limit on the mass ($9\times 10^6 M_\odot$).

- We determine from surface density and size-linewidth parameters that the cloud is not in free-fall or virial equilibrium, and so must be subject to a high external pressure, $P/k \gtrsim 10^8$ K cm^{-3}, if it is a bound structure. A comparison with young massive clusters in NGC 253 that have detected

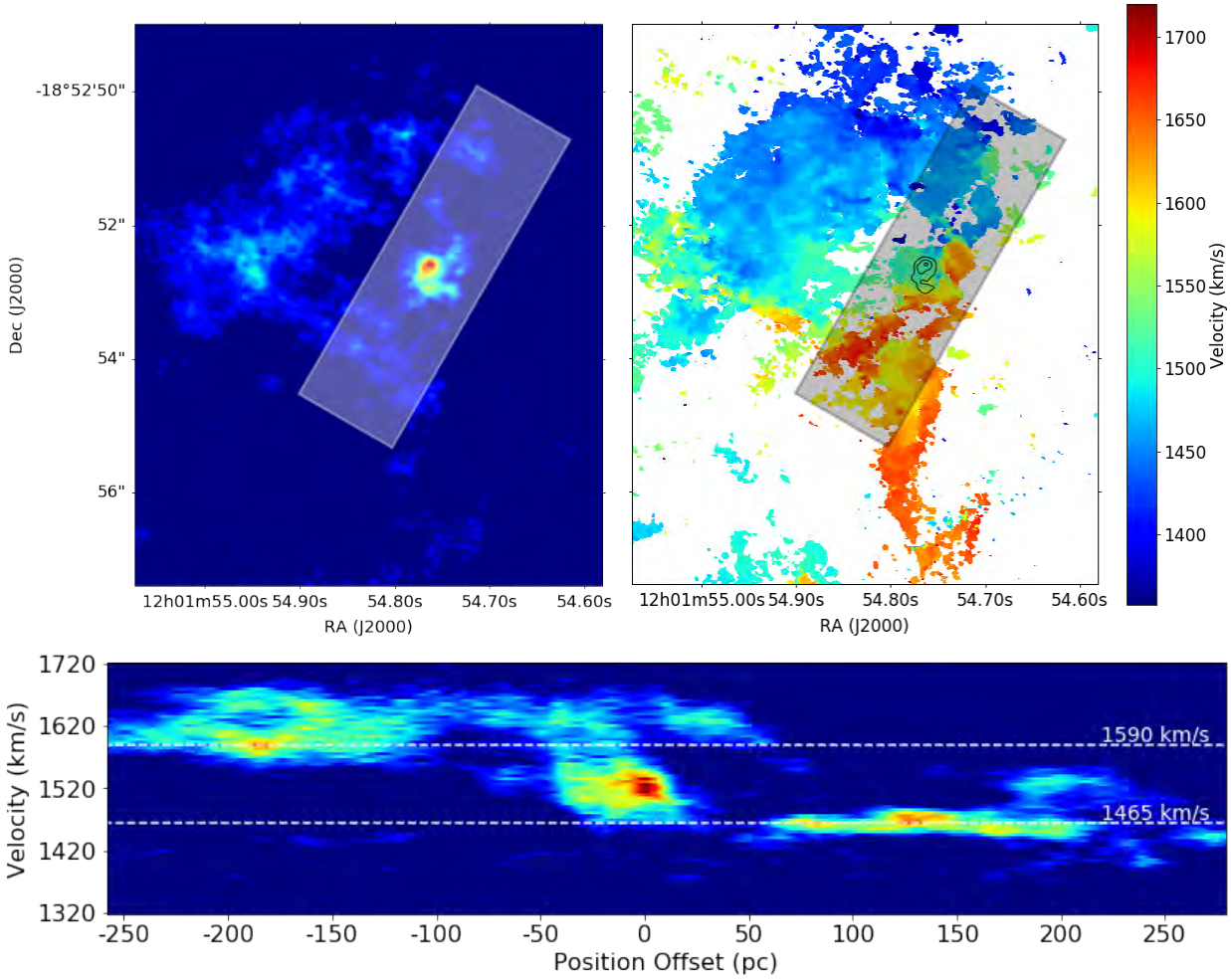

Figure 5: *Top Left:* Moment 0 map of the Firecracker and the surrounding region, with the cut for the position-velocity diagram over plotted as a white rectangle. *Top Right:* Moment 1 map of the same region, with the same cut shown as a gray rectangle. Contours of the moment 0 of the Firecracker cloud are shown in black. *Bottom:* Position-velocity diagram of the Firecracker from the cut shown above. The Firecracker cloud is seen in the center, and appears to be a 'bridge' between the clouds on either side, from the top left of the plot to the bottom right. The velocities of the colliding clouds are shown with the dotted lines, suggesting a relative collision velocity of ~ 125 km s^{-1}.

star formation suggests a potential trend in which clusters with a low $M_{\rm gas}/M_*$ ratio (and so are likely more evolved) are near virial equilibrium or free fall, while clusters with a higher $M_{\rm gas}/M_*$ would require similar high pressures to remain bound. This would agree with theoretical predictions that high pressure environments are necessary for cluster formation. It also agrees with the Bonnor-Ebert fit's prediction that the cloud is pressure-bound and gravitationally stable.

- The position-velocity diagram of the Firecracker and its surrounding cloud shows what may be a "broad bridge" feature, which is indicative of cloud-cloud collision. An estimate of the density and relative velocity of the colliding filaments suggests that they are capable of producing a ram pressure of $\sim 1.1 \times 10^9$ K cm^{-3}, consistent with the high pressures needed for the cloud to be bound.

Acknowledgments

This work was aided by VSGC funding.

References

Ashman, K. M., & Zepf, S. E. 2001, ApJ, 122:4, 1888

Elmegreen, B. G., & Efrefmov, Y. N. 1997, ApJ, 480:1, 235

Fall, S. M., & Zhang, Q. 2001, ApJ, 561:2, 751

Field, G. B., Blackman, E. G., & Keto, E. R. 2011, MNRAS, 416:1, 710

Gerner, T., Beuther, H., & Semenov, D., e. a. 2014, A&A, 563, 97

Harris, W. E., & Pudritz, R. E. 1994, ApJ, 429:1, 177

Haworth, T. J., Tasker, E. J., & Fukui, Y., e. a. 2015, MNRAS, 450, 10

Herrera, C. N., Boulanger, F., Nesvadba, N. P. H., & Falgarone, E. 2012, A&A, 538, 9

Herrera, C. N., Boulanger, R., & Nesvadba, N. P. H. 2011, A&A, 534, 138

Heyer, M., Krawczyk, C., Duval, J., & Jackson, J. M. 2009, ApJ, 699:2, 1092

Johnson, K. E., Leroy, A. K., & Indebetouw, R., e. a. 2015, ApJ, 806:1, 35

Kroupa, P., Aarseth, S., & Hurley, J. 2001, MNRAS, 321:4, 699

Leroy, A. K., Bolatto, A. D., & Ostriker, E. C., e. a. 2018, ApJ

Mangum, J. G., & Shirley, Y. L. 2015, PASP, 127:949, 226

McLaughlin, D. E., & Fall, S. M. 2008, ApJ, 679:2, 1272

O'Connell, R. W., Gallagher, J. S., I., & Hunter, D. A. 1994, ApJ, 433:1, 65

Oey, M. S., Herrera, C. N., & Silich, S., e. a. 2017, ApJL, 849, L1

Turner, J. L., Consiglio, S. M., & Beck, S. C., e. a. 2017, ApJ, 846, 73

van den Bergh, S., Morbey, C., & Pazder, J. 1991, ApJ, 375, 594

Wei, L. H., Keto, E., & Ho, L. C. 2012, ApJ, 750:2, 136

Whitmore, B. C. 2000, in STScI Symposium Series, ed. M. Livio, 14

Whitmore, B. C., Brogan, C., & Chandar, R., e. a. 2014, ApJ, 795:2, 156

Wilson, C. D., Petitpas, G. R., & Iono, D., e. a. 2008, ApJS, 178:2, 189

Zhu, M., Seaquist, E. R., & Kuno, N. 2003, ApJ, 588:1, 243